



# Design and motion analysis of axisymmetric 3D origami with generic six-crease bases<sup>☆</sup>

Yan Zhao\*, Yoshihiro Kanamori, Jun Mitani

*University of Tsukuba, 1-1-1 Tennoh-dai, Ibaraki 305-0006, Japan*

## ARTICLE INFO

### Article history:

Received 12 October 2016

Received in revised form 16 July 2017

Accepted 25 October 2017

Available online xxxx

### Keywords:

Computational origami

Axisymmetric structure

Kinematic behavior

Applications

## ABSTRACT

Origami, also known as paper folding, has shown its potential to construct 3D structures from designed crease patterns on a flat sheet. This paper proposes a method to design axisymmetric 3D origami with generic six-crease bases. Inspired by the conventional six-crease bases, i.e., waterbomb base or Yoshimura base, where six regular crease lines meet at an interior vertex, we generalize the generic base so that the lengths of the crease lines can be regular or irregular. This method is based on designing the crease patterns. First, we interactively generate a crease pattern consisting of such generic bases. Then, our method analytically calculates the 3D origami shape with an axisymmetric structure. We demonstrate various configurations, i.e., sets of input parameters, to explore the variations of the calculated 3D origami. The 3D origami can have multiple degrees of freedom, but by continually changing one parameter we present a motion that can axisymmetrically deploy or flatten the shape. The method for designing 3D origami has potential applications ranging from self-folding tessellations to deployable architectures.

© 2017 Elsevier B.V. All rights reserved.

## 1. Introduction

Origami, also known as paper folding, has received much attention in geometry, mathematics, and engineering. An origami (e.g., Fig. 1 (b)) can be defined by its crease pattern (e.g., Fig. 1 (a)), which contains a set of mountain folded lines (shown in red) and valley folded lines (shown in blue) appearing on a sheet of paper when the origami is opened flat (Mitani, 2011a).

Among the crease patterns, a waterbomb pattern (Fig. 1 (a)) and Yoshimura pattern (Fig. 1 (c)) with interior vertices having six-crease lines are widely used and have been widely researched. For a waterbomb pattern, Tachi et al. (2012) worked on the rigidity of a six-crease origami tessellation to achieve an adaptive freeform surface. Kuribayashi et al. (2006) made the first origami stent to achieve a large deployable ratio. Based on such pattern, a worm robot (Onal et al., 2013) and a deformable wheel robot (Lee et al., 2013) were also proposed. Chen et al. (2016) proposed a comprehensive kinematic analysis on a waterbomb origami with one degree of freedom (DOF) motion under symmetric folding.

A Yoshimura pattern, also known as the diamond pattern (Yoshimura, 1951; Hunt et al., 2003; Thompson et al., 1985) is another crease pattern with interior vertices having six-crease lines. For this pattern, Foster and Krishnakumar (1987) proposed a family of foldable structures. De Temmerman et al. (2007) proposed a concept for a mobile shelter.

\* This paper has been recommended for acceptance by Daniele Panozzo.

Corresponding author.

E-mail address: [yanzhao.npal.tsukuba@gmail.com](mailto:yanzhao.npal.tsukuba@gmail.com) (Y. Zhao).

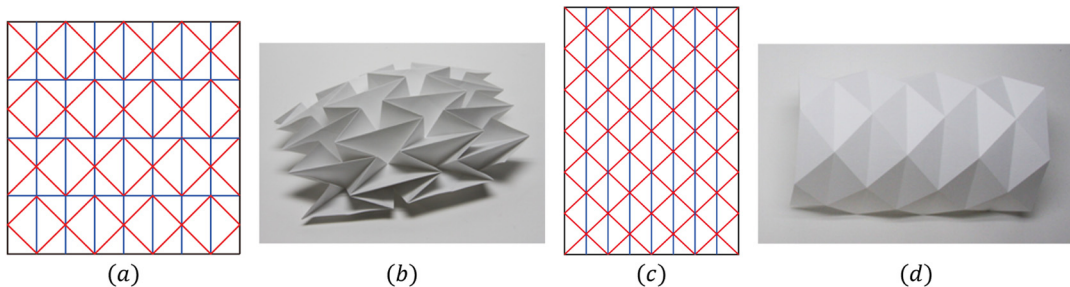


**Fig. 1.** Origami with interior vertices having six-crease lines. (For interpretation of the references to color in this figure, the reader is referred to the web version of this article.)

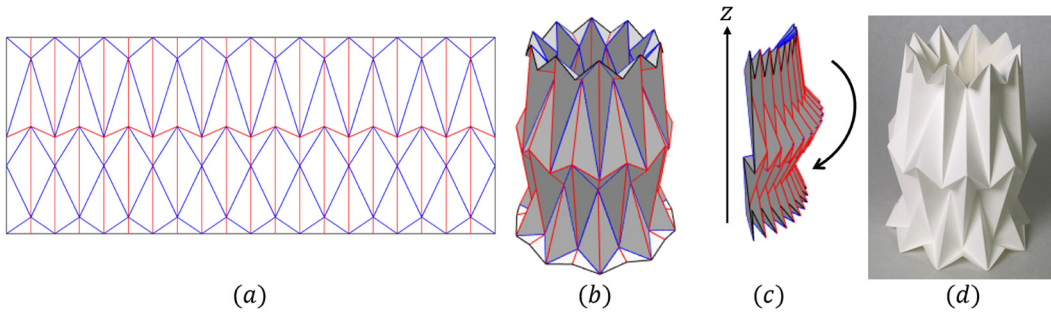


**Fig. 2.** Overview of our method.

Thrall and Quaglia (2014) gave a historical review of origami-like deployable shelters developed by the US military. Cai et al. (2016) investigated the motion of the foldable barrel vault structure based on the regular and irregular Yoshimura pattern.

In this paper, inspired by the six-crease base, which we can be seen from the waterbomb pattern and Yoshimura pattern where six regular crease lines meet at a vertex, we present our generalization of the base, enabling the lengths of the crease lines to be regular or irregular. This method is based on designing the crease patterns. First, we interactively generate a crease pattern consisting of such generic bases (Fig. 2 (a)). Then, our method analytically calculates the 3D origami shape with an axisymmetric structure (Fig. 2 (b)). Finally, while referring to the shape of the 3D origami, the user can fabricate the 3D origami piece (Fig. 2 (d)).

Rigidly foldable origami allows for motion where all facets remain rigid, and deflection only occurs at the crease lines. A rigidly foldable origami can be made of thick materials other than paper. 3D origami consisting of triangular facets has multiple DOFs (Tachi, 2010a), but by continually changing one parameter we present a motion that can axisymmetrically deploy or flatten the shape around the z axis (Fig. 2 (c)). The designed 3D origami has potential applications ranging from self-folding tessellations to deployable architectures.

## 2. Related work

Origami has advanced significantly based on the development of mathematical theories and more computational resources (Wang-Iverson et al., 2016; Demaine and O'Rourke, 2007). TreeMaker is software used to design flat-foldable origami (Lang, 2016). Its basic concept was first introduced by Meguro (1991) and fully described by Lang (1996). This software generates the crease pattern from a graph tree that represents the base structure of the object by using a circle/river packing technique. Tess is another computer program that makes crease patterns for origami tessellations involving twist folds in a repeating pattern (Bateman, 2016). These approaches focus on flat-foldable origami, but we are aiming at making 3D origami.

The *Origamizer* algorithm by Tachi (2010b) is a very general approach that generates a crease pattern for an arbitrary 3D triangle mesh model with a topological disc condition. The approach is based on the tucking technique, which hides the unnecessary areas of a sheet of paper inside the shape. Although the *Origamizer* can handle axisymmetric origami, the generated crease pattern might be over complicated for a simple model.

Mitani proposed a method for designing 3D origami based on a rotational sweep (Mitani, 2009, 2011b), which generates a simpler crease pattern for an axisymmetric structure by adding flaps outside of the target shape. Although the flaps might be considered obtrusive, his method succeeds in generating 3D curved origami. His other method (Mitani, 2012), which combines the advantages of the rotational sweep and mirror reflection approaches, has been used to build geometrically attractive origami pieces. Even though these methods can handle the axisymmetric structure of origami, they cannot adequately handle axisymmetric 3D origami consisting of triangular facets.

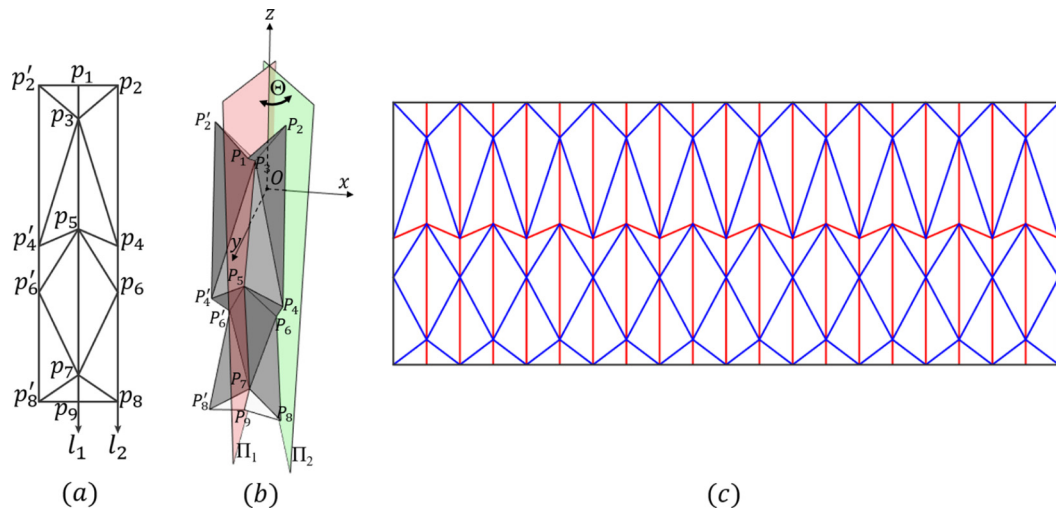


**Fig. 3.** Designing crease pattern.

Zhao et al. (2017) proposed a method to handle a family of axisymmetric 3D origami consisting of triangular facets. This method first designs a rotationally-symmetric crease pattern and then calculates the axisymmetric 3D shape of the origami based on geometric constraints. In this paper, we propose a new method to calculate the axisymmetric 3D origami based on a mirror-symmetric crease pattern.

Dudte et al. (2016) worked on generalized Miura-ori tessellations. This method constructs tessellations for surfaces of negative, positive, and mixed Gaussian curvature. Schenk and Guest (2012) considered a ‘global’ Gaussian curvature of an equivalent mid-surface of the Miura and Eggbox sheets. They found that both sheets can modify their global Gaussian curvature, with no stretching at the material level. On the application side, Zirbel et al. (2013, 2015) proposed a method to build a large solar array for space applications. Filipov et al. (2016) proposed a class of origami tubes. The 3D origami proposed by Zhao et al. (2017) could be applied to build an origami dome.

### 3. Designing 3D origami

#### 3.1. Designing crease pattern

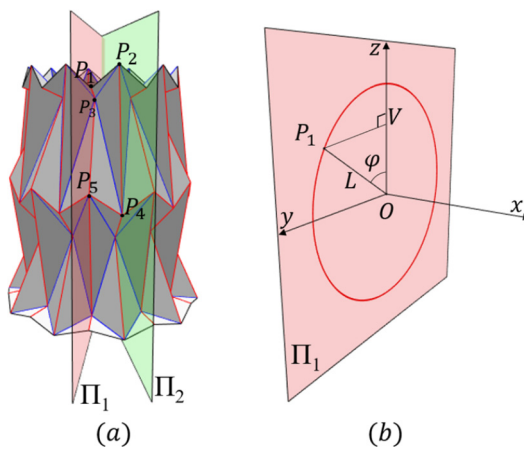
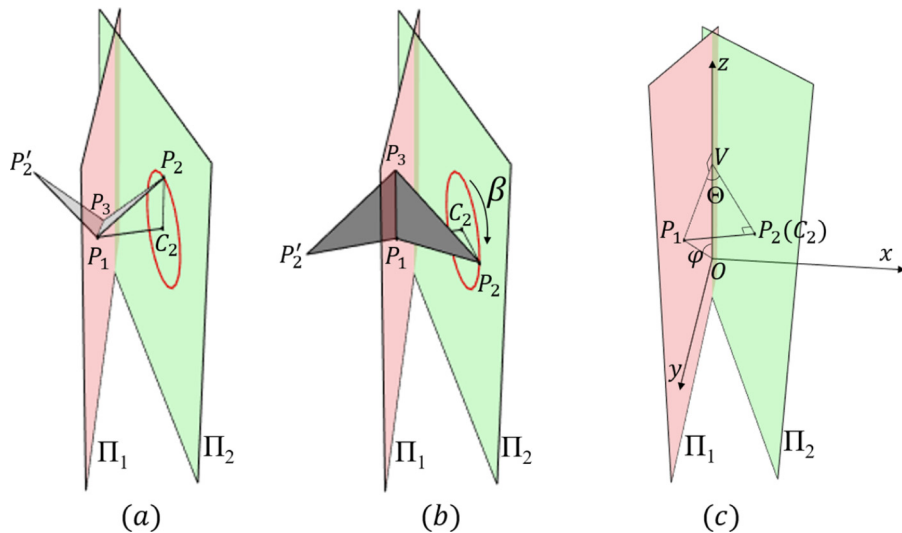
In this section, we describe the crease pattern made using generic six-crease bases. Fig. 3 (a) shows a  $1/N$  part of the crease pattern (where  $N$  indicates the order of rotational symmetry and equals 10 in this example), (b) shows the corresponding part in 3D space.  $p_i (i = 1, 2, 3, \dots)$  denote the points in the 2D crease pattern, and  $P_i (i = 1, 2, 3, \dots)$  indicate the corresponding points in 3D space.  $l_1$  and  $l_2$  are two parallel lines.  $p_i$  (with odd indices) lie on line  $l_1$  and  $p_i$  (with even indices) lie on line  $l_2$ .  $p'_i$  (with even indices) are the symmetric points of  $p_i$  with respect to line  $l_1$ . The crease pattern can be interactively designed. Specifically, we can adjust the space between lines  $l_1$  and  $l_2$ . We can also move, add, and delete  $p_i$  along lines  $l_1$  or  $l_2$ . For a newly added  $p_i (i > 2)$ , we place crease lines  $p_i p_{i-1}$  and  $p_i p_{i-2}$ , to guarantee that all interior points have valence six. After the  $1/N$  part of the crease pattern is specified, we generate the whole crease pattern by repeating the  $1/N$  part  $N$  times (Fig. 3 (c)).

Fig. 3 (b) illustrates the overall layout of the pattern in 3D space.  $O$  is the origin of a Cartesian coordinate system.  $\Pi_1$  is a vertical plane passing through the  $z$  axis and  $y$  axis.  $\Pi_2$  is another vertical plane passing through the  $z$  axis.  $\Theta$ , which equals  $180^\circ/N$ , is an angle between such two vertical planes.  $P_i$  (with odd indices) lie on the plane  $\Pi_1$  and  $P_i$  (with even indices) lie on the plane  $\Pi_2$ .  $P'_i$  and  $P_i$  (with even indices) are symmetric with respect to plane  $\Pi_1$ . After the  $1/N$  part of the 3D origami is calculated, we achieve the axisymmetric 3D origami by iteratively rotating its  $1/N$  part about the  $z$  axis.

We also introduce a parameter  $T$  to represent the number of editable points in the  $1/N$  part of the crease pattern (e.g.,  $T = 9$  in Fig. 3 (a)). Note that every interior vertex having six crease lines has a mirror-symmetric property. We can make the six crease lines of the interior vertex irregular (e.g.,  $|p_3 p_1| \neq |p_3 p_5|$  and  $|p_3 p_2| \neq |p_3 p_4|$  at  $p_3$ ) because  $p_i$  are interactively moved in the crease pattern. Using such a crease pattern consisting of regular or irregular six-crease bases, we can generate novel 3D origami (e.g., the origami pieces shown in Fig. 12).

#### 3.2. Calculation of each 3D point

In this section, we take the generated  $1/N$  part of the crease pattern (shown in Fig. 3(a)) as input and describe a method to calculate each point on 3D origami based on geometric constraints.  $P_i$  is calculated sequentially in the order of its index. First, we use Eq. (1) to define  $P_1$  on the plane  $\Pi_1$  (Fig. 4 (b)).

Fig. 4. Determination of  $P_1$ .Fig. 5. Calculation of  $P_2$ .

$$P_1 = (0, L \sin(\varphi), L \cos(\varphi)), \quad (1)$$

where  $L$  indicates the length of  $|OP_1|$  and  $\varphi$  represents the angle between  $OP_1$  and the  $z$  axis. As shown in Fig. 4,  $\varphi$  is set as  $58^\circ$  for generating (a).  $V$  is the foot of the perpendicular from  $P_1$  to the  $z$  axis.

Next, we calculate the 3D coordinates of  $P_2$  based on the following constraints: (i) the distance between  $P_2$  and  $P_1$  should be the same as  $|p_2 p_1|$  in the crease pattern, (ii)  $P_2$  should lie on the plane  $\Pi_2$ . To satisfy these two constraints, we achieve candidates for  $P_2$ , which are gathered on the solution circle shown in red, the center of which is represented as  $C_2$  (Fig. 5 (a) and (b)). To achieve one solution of  $P_2$ , we introduce a parameter denoted as  $\beta$ , which is the angle between  $C_2 P_2$  and the  $z$  axis. By specifying the angle  $\beta$  ranging from  $0^\circ$  to  $360^\circ$ , we can obtain various  $P_2$ , as examples shown in Fig. 5 (a) and (b), where  $\beta$  equals  $0^\circ$  and  $90^\circ$ , respectively. The solution circle shown in red is an intersection of the plane  $\Pi_2$  and a sphere, the center of which is  $P_1$  and the radius of which equals  $|p_1 p_2|$ . Here, we introduce an upper bound of  $L$  as  $L_b$ , when the solution circle degenerates to one point  $C_2$  (Fig. 5 (c)).  $L_b$  can be defined as Eq. (2) in right triangle  $OP_1V$ .

$$L_b = \frac{|VP_1|}{\sin(\varphi)}. \quad (2)$$

Meanwhile,  $|VP_1|$  is defined as Eq. (3) in right triangle  $VP_2P_1$ .

$$|VP_1| = \frac{|P_1P_2|}{\sin(\Theta)}. \quad (3)$$

By substituting Eq. (3) for Eq. (2), we can obtain  $L_b$  in Eq. (4):

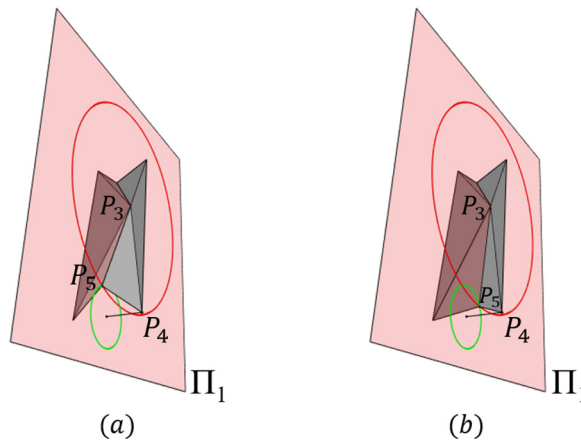


**Fig. 6.** Calculation of  $P_i (i > 2)$ , where  $i = 5$ .

$$L_b = \frac{|P_1 P_2|}{\sin(\Theta) \sin(\varphi)} = \frac{|p_1 p_2|}{\sin(180^\circ/N) \sin(\varphi)}. \quad (4)$$

Note that  $|p_1 p_2|$  and  $N$  are given by the crease pattern, and thus for a given crease pattern  $L_b$  is related to another input  $\varphi$ .

Next, we calculate the 3D coordinates of  $P_i (i > 2)$  based on the following constraints: (i) the distance between  $P_i$  and  $P_{i-1}$  should be the same as  $|p_i p_{i-1}|$  in the crease pattern, (ii) the distance between  $P_i$  and  $P_{i-2}$  should be the same as  $|p_i p_{i-2}|$  in the crease pattern, (iii)  $P_i$  should lie on the plane  $\Pi_1$  (for an odd index) or  $\Pi_2$  (for an even index).

We set  $i = 5$  and describe the calculation of  $P_5$  (Fig. 6).  $P_5$  lies on the plane  $\Pi_1$  and is connected to  $P_4$  and  $P_3$ . First, by considering the distance constraint between  $P_5$  and  $P_4$ , we achieve the candidates that are gathered on the circle shown in green. Second, by considering the distance constraint between  $P_5$  and  $P_3$ , we obtain the candidates that are gathered on the circle shown in red. Finally, two intersection points between the two circles (the red one and the green one) that satisfy all the constraints at the same time are selected as two candidates for  $P_5$  (if they exist). Our system gives feedback when no candidates achieved and allows us to select when two candidates exist. By selecting either of them, we can generate different shapes of 3D origami (Fig. 6 (a) and (b)). After all  $P_i$  and  $P'_i$  (with even indices) are calculated, we achieve the  $1/N$  part of the 3D origami. Then, by iteratively rotating such 3D part about the z axis, we can obtain the resultant shape of 3D origami (Fig. 4 (a)). Finally, based on the generated 3D model, we determine the mountain and valley assignments on its crease pattern (Fig. 3 (c)).

The space of 3D origami consisting of triangular facets could be very rich. For a calculated 3D origami (whose crease pattern and choices for selecting 3D candidates are determined), we explore its variations by changing parameters  $\varphi$ ,  $L$ , and  $\beta$  in the discrete domain. We refer to a set of  $\varphi$ ,  $L$ , and  $\beta$  as a configuration. We set a range of  $\varphi$  from  $0^\circ$  to  $180^\circ$  without  $0^\circ$  and  $180^\circ$ , because we cannot achieve  $L_b$  when  $\varphi$  equals such two values.  $L$  ranges from 0 to  $L_b$  for a given  $\varphi$  (Eq. (4)). The value of  $\beta$  ranges from  $0^\circ$  to  $360^\circ$ .

Here, for the 3D origami shown in Fig. 12 (a), we demonstrate various configurations as points (Fig. 7 (a)) that represent 3D origami pieces achievable without self-intersections. The crease pattern and choices for selecting 3D candidates are remained during the exploration. To normalize  $L$ , we introduce  $L_{max}$ , found in the experiment, which indicates the maximum of  $L$  that exists at least one configuration for generating achievable 3D origami. Specifically, we demonstrate 18 samples (Fig. 7 (b), (c), and (d)) and their corresponding 3D shapes (Fig. 7 (e)). We achieve 3D shapes from #1 to #6 by increasing  $\varphi$  from  $21^\circ$  to  $86^\circ$  while keeping  $L$  and  $\beta$  remained as  $2.56e-2 L_{max}$  and  $36^\circ$ , respectively. By increasing  $L$  from  $0.95e-2 L_{max}$  to  $3.34e-2 L_{max}$ , we achieve 3D shapes from #7 to #12, where  $\varphi$  and  $\beta$  are fixed as  $106^\circ$  and  $36^\circ$ , respectively. We can also achieve 3D shapes from #13 to #18, by increasing  $\beta$  from  $157^\circ$  to  $167^\circ$  while keeping  $\varphi$  and  $L$  remained as  $61^\circ$  and  $2.59e-2 L_{max}$ , respectively.

#### 4. Motion analysis

In this section, we describe an along-circumference flat-folding, which is triggered by parameter  $\Theta$ , the angle between planes  $\Pi_1$  and  $\Pi_2$ .

##### 4.1. Calculation of degree of freedom

The degrees of freedom of a triangular mesh are represented as Eq. (5)

$$DOF = N_{Eo} - 3N_L - 3, \quad (5)$$

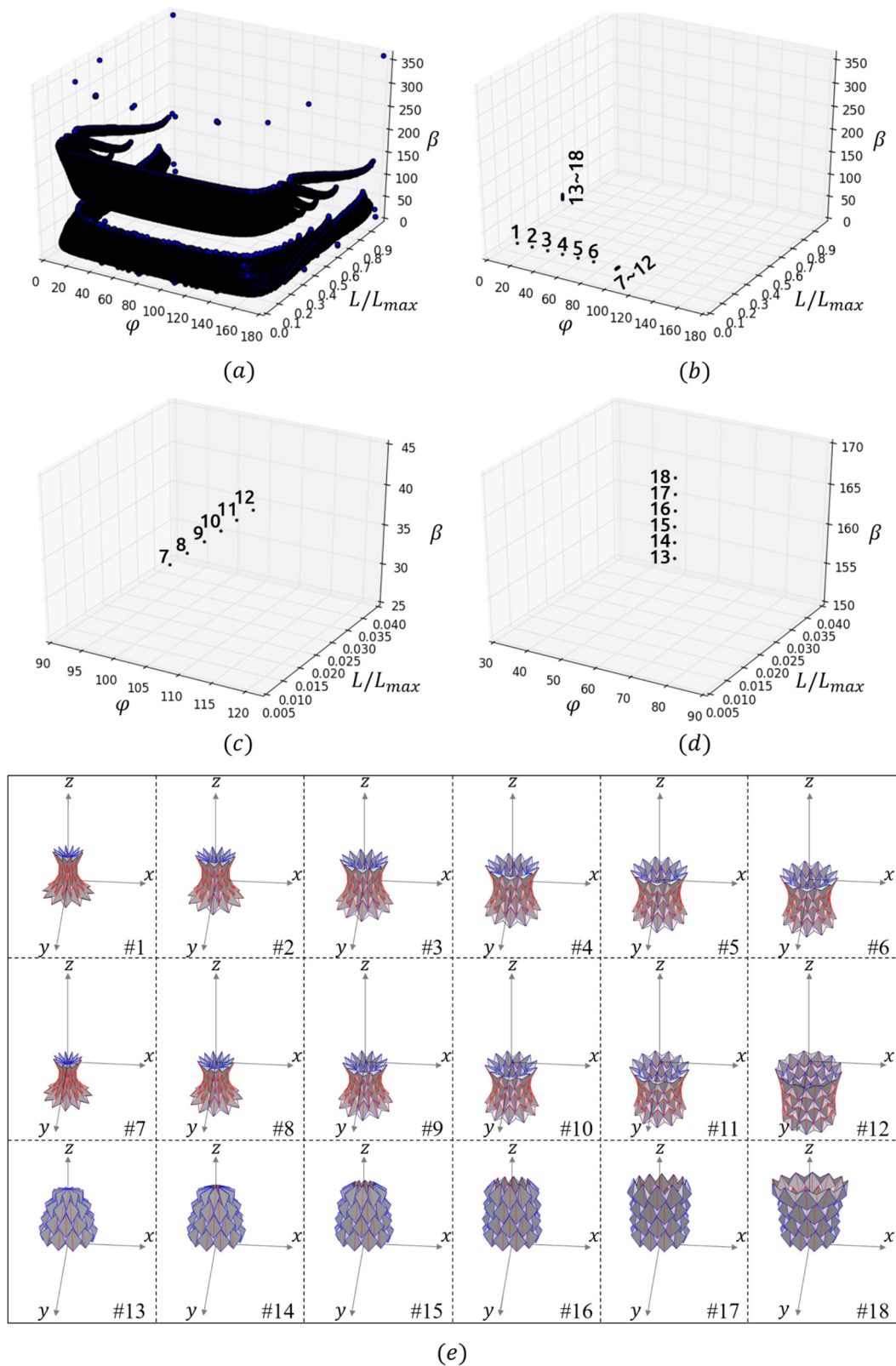
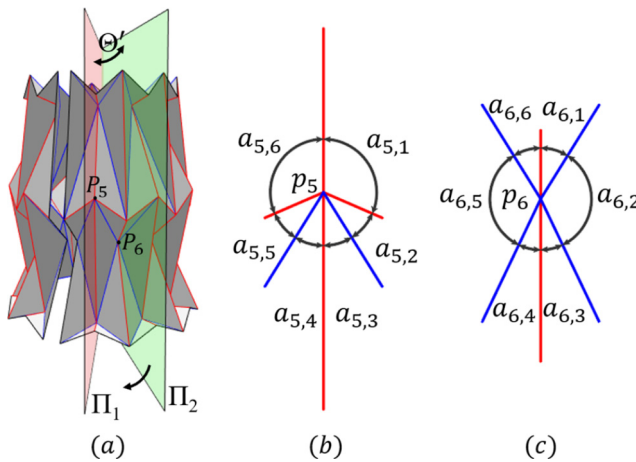
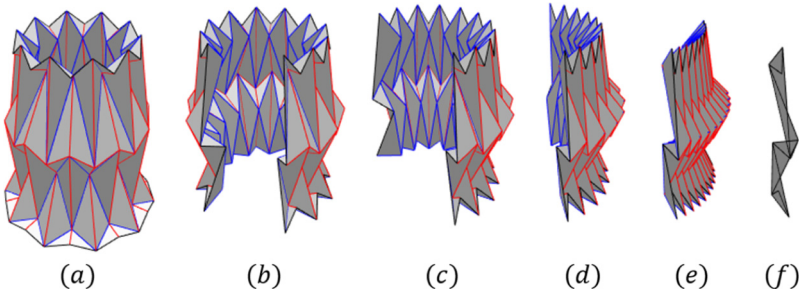


Fig. 7. Variations in 3D origami by changing configuration.



**Fig. 8.** Satisfaction of Kawasaki's theorem for each interior vertex.



**Fig. 9.** Along-circumference flat-folding with self-intersection-free test.

where  $N_{Eo}$  is the number of edges on the boundary, and  $N_L$  is the number of holes (Tachi, 2010a). In our work,  $N_{Eo}$  is represented by Eq. (6)

$$N_{Eo} = 4N + 2\left(\left\lfloor \frac{T}{2} \right\rfloor - 1\right), \quad (6)$$

where  $N$  indicates the order of rotational symmetry, and  $T$  represents the number of editable points in the  $1/N$  part of the crease pattern. In addition,  $N_L$  equals zero, thus the degrees of freedom in our work are represented as

$$DOF = 4N + 2\left(\left\lfloor \frac{T}{2} \right\rfloor - 1\right) - 3. \quad (7)$$

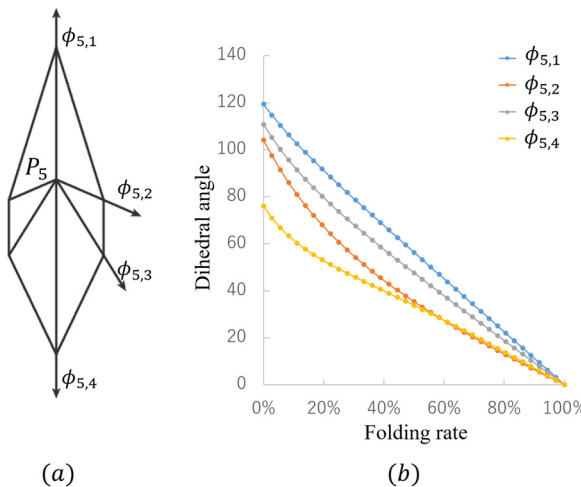
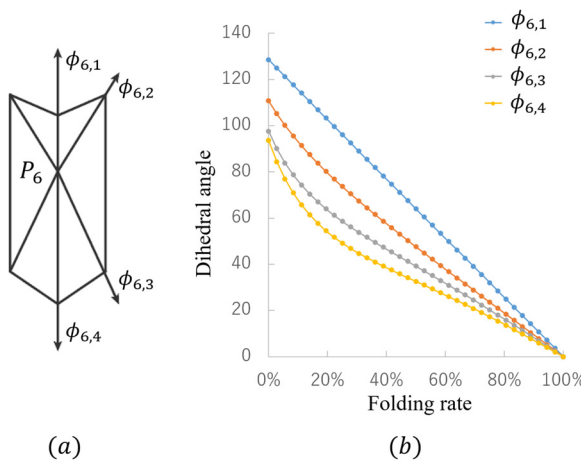
According to Eq. (7), the 3D origami in Fig. 8 (a) has 43 DOFs ( $N = 10$  and  $T = 9$ ).

Within those DOFs, we can axisymmetrically flat fold the 3D origami with decreasing angle  $\Theta$ . Specifically,  $P_i$  (with even indices) on plane  $\Pi_2$  together with the symmetric  $P'_i$  fall towards plane  $\Pi_1$  with decreasing  $\Theta$  (represented as  $\Theta'$ ,  $0^\circ \leq \Theta' \leq \Theta$ , in Fig. 8 (a)). For the whole origami, such a process compresses the 3D shape towards plane  $\Pi_1$ . Meanwhile, the 3D origami is locally flat-foldable based on the satisfaction of Kawasaki's theorem (Kawasaki, 1989). Kawasaki's theorem provides a necessary criterion for an origami construction to be flat, which states that a collection of creases meeting at a vertex are flat-foldable if and only if the sum of the alternate angles around the vertex is  $180^\circ$ . Here, we show the interior vertices  $p_5$  and  $p_6$  (Fig. 8 (b) and (c)), for which the 3D points  $P_5$  and  $P_6$  are convex and concave, respectively. Angle  $\alpha_{i,k}$  denotes the  $k$ -th incident sector angle of  $p_i$ . For  $p_5$ , because  $\alpha_{5,1} = \alpha_{5,6}$ ,  $\alpha_{5,2} = \alpha_{5,5}$ , and  $\alpha_{5,3} = \alpha_{5,4}$ ,  $\alpha_{5,1} + \alpha_{5,3} + \alpha_{5,5} = \alpha_{5,2} + \alpha_{5,4} + \alpha_{5,6} = 180^\circ$ , satisfying Kawasaki's theorem. Similarly, we can show that  $p_6$  also satisfies Kawasaki's theorem (Fig. 8 (c)). In general, interior vertices satisfy Kawasaki's theorem because they have a mirror-symmetric property.

To intuitively describe the folding state due to angle  $\Theta'$ , we introduce a folding rate:

$$FR = 100(1 - \frac{\Theta'}{\Theta})\%. \quad (8)$$

Fig. 9 shows the along-circumference flat-folding where the folding rate equals 0%, 20%, 40%, 60%, 80%, and 100% corresponding to (a), (b), (c), (d), and (f), respectively. The origami remains rigid in this folding sequence, which is triggered by continually changing  $\Theta'$ . Self-intersections could occur during the motion. Here, we enumerate the folded 3D shapes

**Fig. 10.** Kinematic behavior of  $P_5$ .**Fig. 11.** Kinematic behavior of  $P_6$ .

based on  $\Theta'$ , ranging from  $\Theta$  to  $0^\circ$  in the discrete domain with dense sampling. The folding sequence is considered as self-intersection-free when none of the enumerated 3D shapes has self-intersections.

#### 4.2. Kinematic behavior

We analyzed the kinematic behavior of the vertices in a designed 3D origami during motion. For the origami shown in Fig. 8 (a), without loss of generality, we selected a convex  $P_5$  that has four mountain and two valley folded lines and a concave  $P_6$  that has two mountain and four valley folded lines for analysis. We introduced angle  $\phi_{i,k}$  indicating the  $k$ -th dihedral angle at vertex  $P_i$ , and  $k$  is started from one and assigned clockwise (Fig. 10 (a) and Fig. 11 (a)). The relationship between the folding rate and dihedral angles at selected vertices  $P_5$  and  $P_6$  during motion are illustrated in Fig. 10 (b) and Fig. 11 (b), respectively.

The maximum dihedral angles at  $P_5$  are  $119^\circ$ ,  $104^\circ$ ,  $111^\circ$ , and  $76^\circ$  corresponding to  $\phi_{5,1}$ ,  $\phi_{5,2}$ ,  $\phi_{5,3}$ , and  $\phi_{5,4}$ , respectively. For  $P_6$ , the maximum dihedral angles are  $129^\circ$ ,  $111^\circ$ ,  $98^\circ$ , and  $94^\circ$  corresponding to  $\phi_{6,1}$ ,  $\phi_{6,2}$ ,  $\phi_{6,3}$ , and  $\phi_{6,4}$ , respectively. The knowledge of these maximum dihedral angles helped us to build a rigid origami structure with double layered thick composite panels because it is a factor to avoid collision between panels (Tachi, 2010a). In addition, based on the kinematic analysis during motion, we could control the dihedral angles by setting actuators to build self-folding tessellations or deployable architectures.

## 5. Results

We show several resulting origami pieces in Figs. 12 and 13, where the first column shows the crease patterns, the second column shows the 3D models, and the third column shows the photo of the origami pieces. Fig. 12 shows (a) a can-

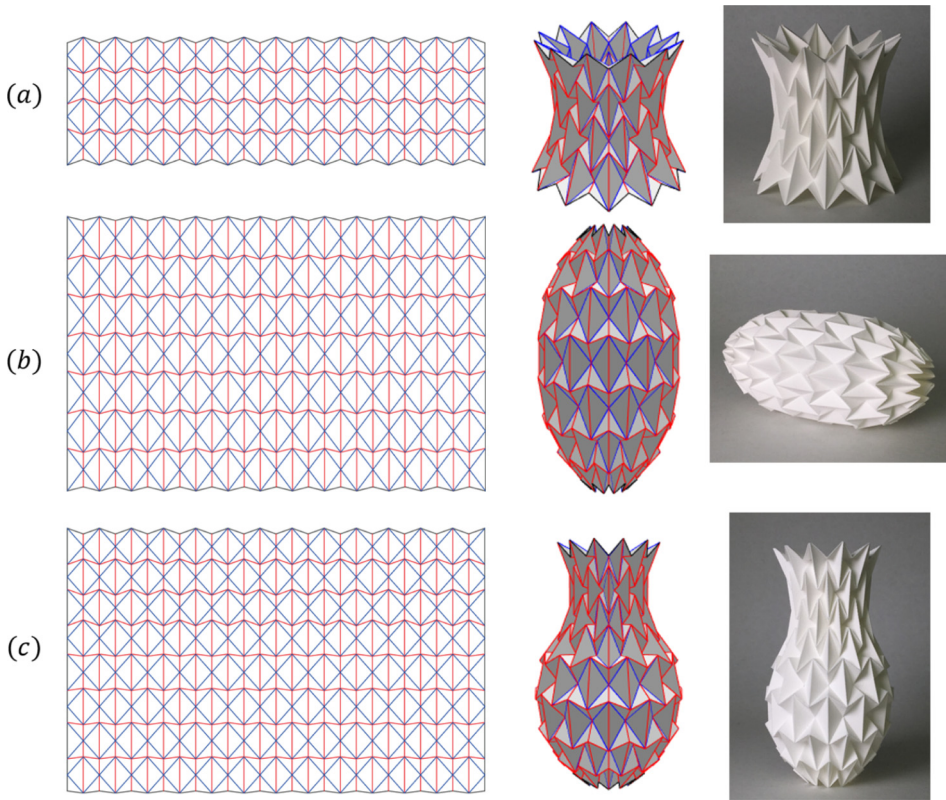


**Fig. 12.** Resulting origami pieces with different 'global' Gaussian curvature.

dlestick with a negative global Gaussian curvature, (b) a rugby ball with a positive global Gaussian curvature, and (c) a vase with a curved base having a positive global Gaussian curvature and a curved neck having a negative global Gaussian curvature. Here, our interest lies in the macroscopic behavior of the sheets, and thus we consider the global Gaussian curvature (Schenk and Guest, 2012) of an equivalent mid-surface of the folded sheet.

Fig. 13 shows (a) a lampshade and (b) a bud.  $P_1$  in both of them lie on the symmetric axis. (c) shows another bud, and (d) and (e) show a ball and a cup, respectively. We achieved the folding sequences shown in Fig. 14. Note that  $P_1$  stays on the symmetric axis during motion in Fig. 14 (a).

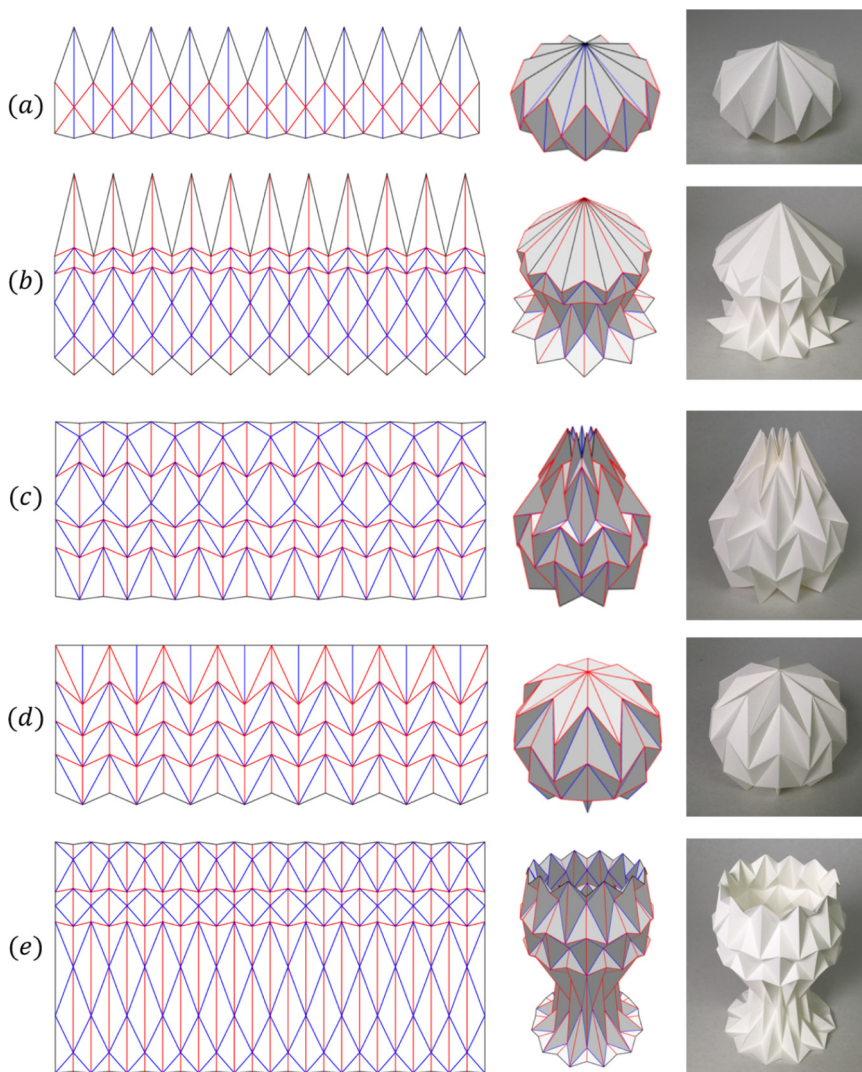
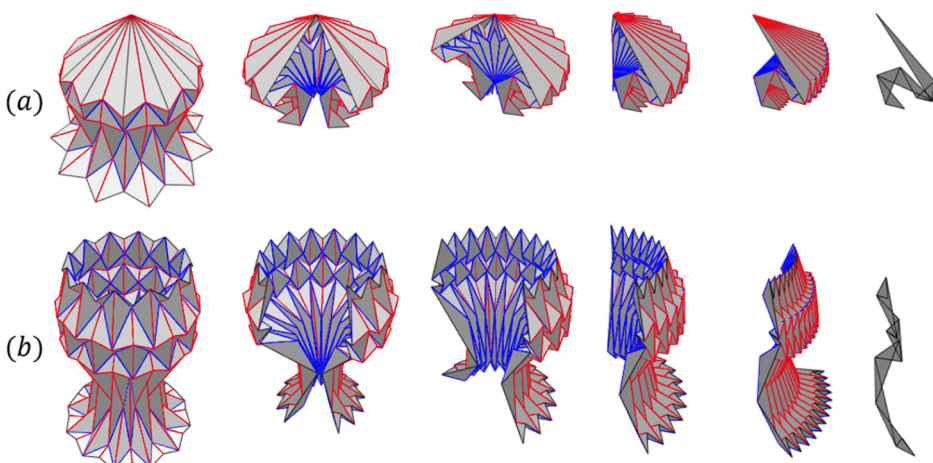
For the 3D origami having self-intersections during the motion, we manually modified the design. Here, we take the 3D origami shown in Fig. 15 (a) as an example. We can see that the facets shown in red penetrated each other (Fig. 15 (b)). In addition, from Fig. 15 (c) showing the relationship between the folding rate and dihedral angles at vertex  $P_5$ , we note that the folding motion is interrupted by self-intersections when the folding rate is larger than 46%. For the origami shown in Fig. 15 (a), we adjust its vertices in crease pattern to achieve the shape shown in Fig. 16 (a). The modified one can be flat folded without self-intersections (Fig. 16 (b) and (c)).

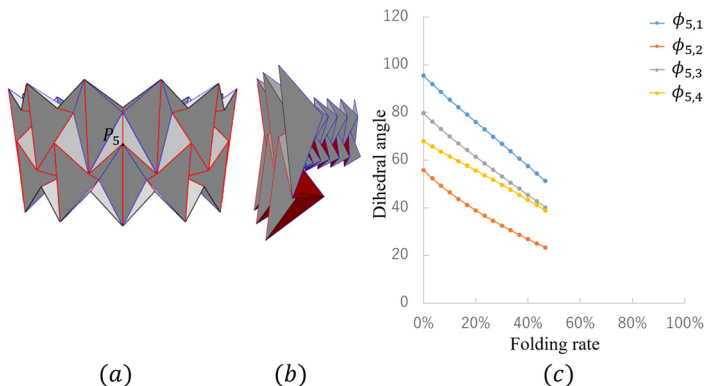
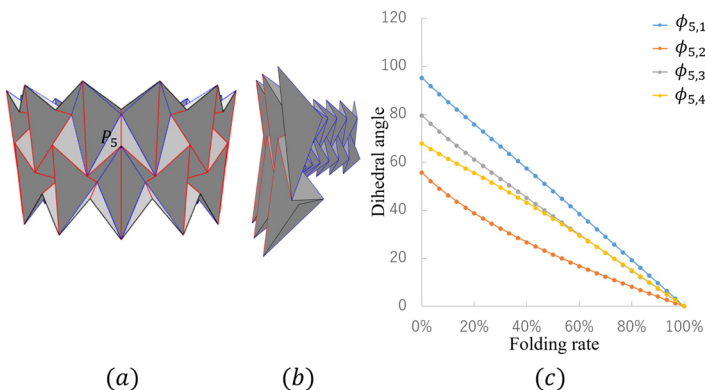
## 6. Conclusion

We described a design method for a class of axisymmetric 3D origami with generic six-crease bases, for which the lengths of the crease lines can be regular or irregular. First, we interactively generate a crease pattern consisting of such generic bases. Then, our method analytically calculates the 3D origami shape with an axisymmetric structure. We demonstrated various configurations to explore the variations of the calculated 3D origami.

We described an along-circumference flat-folding to flat fold the 3D origami axisymmetrically by continually changing parameter  $\Theta$ , the angle between planes  $\Pi_1$  and  $\Pi_2$ . First, we described the calculation of DOF and the folding process triggered by changing  $\Theta$ . We also showed that the 3D origami is locally flat-foldable based on the satisfaction of Kawasaki's theorem for each interior vertex  $p_i$ . Finally, we analyzed the kinematic behavior by illustrating the relationship between the folding rate and dihedral angles at selected vertices on 3D origami. Several origami pieces and folding sequences are presented to demonstrate the validity.

In the future, for 3D origami having self-intersections, we want to automatically revise them as little as possible. On the application side, we intend to build self-folding tessellations or deployable architectures with actuators and thick panels. Furthermore, we hope this work can be extended to create more complex structures by assembling the axisymmetric 3D

**Fig. 13.** Resulting origami pieces.**Fig. 14.** Folding sequences with self-intersection-free test.

**Fig. 15.** Self-intersections occur during folding motion.**Fig. 16.** Modification to enable the origami be flat folded.

origami, and lead us to solve the inverse-origami-design problem, which is to approximate target surfaces of constant or varying curvature using the generic six-crease bases.

## References

- Bateman, A., 2016. Paper mosaic origami tessellations. <http://www.papermosaics.co.uk/software.html>. (Accessed 6 October 2016).
- Cai, J., Deng, X., Xu, Y., Feng, J., 2016. Motion analysis of a foldable barrel vault based on regular and irregular yoshimura origami. *J. Mech. Robot.* 8 (2), 021017.
- Chen, Y., Feng, H., Ma, J., Peng, R., You, Z., 2016. Symmetric Waterbomb Origami. *Proc. R. Soc. A*, vol. 472. The Royal Society, p. 20150846.
- De Temmerman, I.a.N., Mollaert, M., Van Mele, I.a.T., De Laet, I.a.L., 2007. Design and analysis of a foldable mobile shelter system. *Int. J. Space Struct.* 22 (3), 161–168.
- Demaine, E.D., O'Rourke, J., 2007. *Geometric Folding Algorithms*. Cambridge University Press, Cambridge.
- Dudte, L.H., Vouga, E., Tachi, T., Mahadevan, L., 2016. Programming curvature using origami tessellations. *Nat. Mater.* 15, 583–588.
- Filipov, E., Paulino, G., Tachi, T., 2016. Origami Tubes with Reconfigurable Polygonal Cross-Sections. *Proc. R. Soc. A*, vol. 472. The Royal Society, p. 20150607.
- Foster, C., Krishnakumar, S., 1987. A class of transportable demountable structures. *Int. J. Space Struct.* 2 (3), 129–137.
- Hunt, G., Lord, G.J., Peletier, M.A., 2003. Cylindrical shell buckling: a characterization of localization and periodicity. *Discrete Contin. Dyn. Syst., Ser. B* 3 (4), 505–518.
- Kawasaki, T., 1989. On the relation between mountain-creases and valley-creases of a flat origami. In: *Proceedings of the 1st International Meeting of Origami Science and Technology*, pp. 229–237.
- Kuribayashi, K., Tsuchiya, K., You, Z., Tomus, D., Umemoto, M., Ito, T., Sasaki, M., 2006. Self-deployable origami stent grafts as a biomedical application of Ni-rich TiNi shape memory alloy foil. *Mater. Sci. Eng. A* 419 (1), 131–137.
- Lang, R.J., 1996. A computational algorithm for origami design. In: *Proceedings of the Twelfth Annual Symposium on Computational Geometry*. ACM, pp. 98–105.
- Lang, R.J., 2016. Treemaker. <http://www.langorigami.com/article/treemaker/>. (Accessed 6 October 2016).
- Lee, D.-Y., Kim, J.-S., Kim, S.-R., Koh, J.-S., Cho, K.-J., 2013. The deformable wheel robot using magic-ball origami structure. In: *ASME 2013 International Design Engineering Technical Conferences and Computers and Information in Engineering Conference*. American Society of Mechanical Engineers, VO6BT07A040.
- Meguro, T., 1991. The method to design origami, Origami Tanteidan Newspaper.
- Mitani, J., 2009. A design method for 3D origami based on rotational sweep. *Comput.-Aided Des. Appl.* 6 (1), 69–79.
- Mitani, J., 2011a. A method for designing crease patterns for flat-foldable origami with numerical optimization. *J. Geom. Graph.* 15 (2), 195–201.
- Mitani, J., 2011b. A design method for axisymmetric curved origami with triangular prism protrusions. In: *Origami 5: Fifth International Meeting of Origami Science, Mathematics, and Education*, CRC Press, p. 437.
- Mitani, J., 2012. Column-shaped origami design based on mirror reflections. *J. Geom. Graph.* 16 (2), 185–194.
- Onal, C.D., Wood, R.J., Rus, D., 2013. An origami-inspired approach to worm robots. *IEEE/ASME Trans. Mechatron.* 18 (2), 430–438.

- Schenk, M., Guest, S., 2012. Folded Shell Structures. Ph.D. thesis. University of Cambridge, Cambridge, United Kingdom.
- Tachi, T., 2010a. Geometric considerations for the design of rigid origami structures. In: Proceedings of the International Association for Shell and Spatial Structures (IASS) Symposium, vol. 12, pp. 458–460.
- Tachi, T., 2010b. Origamizing polyhedral surfaces. *IEEE Trans. Vis. Comput. Graph.* 16 (2), 298–311.
- Tachi, T., Masubuchi, M., Iwamoto, M., Rigid origami structures with vacuumatics: geometric considerations. Paper presented at IASS-APCS Seoul, Korea, 21–24 May, 2012.
- Thompson, J., Hunt, G., Tvergaard, V., 1985. Elastic instability phenomena. *J. Appl. Mech.* 52 (1), 241–242.
- Thrall, A., Quaglia, C., 2014. Accordion shelters: a historical review of origami-like deployable shelters developed by the US military. *Eng. Struct.* 59, 686–692.
- Wang-Iverson, P., Lang, R.J., Mark, Y., 2016. Origami 5: Fifth International Meeting of Origami Science, Mathematics, and Education. CRC Press.
- Yoshimura, Y., 1951. On the mechanism of buckling of a circular cylindrical shell under axial compression. *Rep. Inst. Sci. Technol., Univ. of Tokyo* 5, 179–198.
- Zhao, Y., Kanamori, Y., Mitani, J., 2017. Geometry of axisymmetric 3D origami consisting of triangular facets. *J. Geom. Graph.* 21 (1), 107–118.
- Zirbel, S.A., Lang, R.J., Thomson, M.W., Sigel, D.A., Walkemeyer, P.E., Trease, B.P., Magleby, S.P., Howell, L.L., 2013. Accommodating thickness in origami-based deployable arrays. *J. Mech. Des.* 135 (11), 111005.
- Zirbel, S.A., Trease, B.P., Thomson, M.W., Lang, R.J., Magleby, S.P., Howell, L.H., 2015. Hanaflex: a large solar array for space applications. In: SPIE Defense+ Security. International Society for Optics and Photonics, p. 94671C.